Integrated Dynamic Aeroelasticity Response Analyses for Multiscale Design Optimization of Unmanned Aerial Vehicle with Blended Wing Body Configuration

Jason Millar[1], Trung Tran[2], Udit Sapre[3], Ryan Miller[4], Kieran Lee[5], Samantha Mosca[6], Mostafa S.A. ElSayed[7], Fidel Khouli[8], and Fred Nitzsche[9]

Carleton University, Ottawa, Ontario, K1S 5B6, Canada

Abstract

The work presented in this paper is developed by the 2018-2019 Blended Wing Body (BWB) Unmanned Aerial Vehicle (UAV) team at Carleton University. The BWB-UAV is a fourth-year capstone project run by the Department of Mechanical and Aerospace Engineering at Carleton University. The purpose of this project is to design, manufacture, test and fly a BWB UAV using both well-established engineering tools and processes adopted by the aerospace industry. Here, multiscale design optimization (MSDO) is employed for the airframe mass minimization and aircraft performance maximization. The MSDO process is implemented in two-stage which combines topological and lattice optimization. While most of the existing developments in aerospace consider a deterministic set of critical load cases for the design optimization process, in this paper, the dynamic aeroelastic response analysis of the UAV is integrated into the MSDO algorithm where the critical loads are periodically updated with variations of mass and stiffness distribution during design optimization. A preliminary Detailed Finite Element Model (DFEM) of the airframe of the UAV is developed and used in the MSDO process. On the other hand, Craig-Bampton model order reduction method is employed to reduce the size the DFEM so it can be conveniently coupled with the Doublet Lattice Aerodynamic Model generating a computationally efficient aeroelasticity module necessary for the iterative dynamic aeroelasticity analyses. Preliminary results indicate that a weight reduction of up to 43% of the baseline airframe is achievable using the proposed optimization process.

Nomenclature

Symbol	Definition
$m(x)$	Airframe Mass
$\bar{\rho}$	Relative Density
V	Volume Fraction
$r_{lattice}$	Lattice min. radius
P	Density penalization
σ_{vM}	von Mises Stress
$S_{allowable}$	Allowable Stress
$SF_{buckling}$	Buckling Safety Factor
ψ_I	Normalized Second Moment of Area
ψ_A	Normal Cross-Sectional Area
λ	Geometric Efficiency

[1] BEng Student, Mechanical and Aerospace Engineering, Carleton University, Ottawa, ON, Canada
[2] BEng Student, Mechanical and Aerospace Engineering, Carleton University, Ottawa, ON, Canada
[3] BEng Student, Mechanical and Aerospace Engineering, Carleton University, Ottawa, ON, Canada
[4] BEng Student, Mechanical and Aerospace Engineering, Carleton University, Ottawa, ON, Canada
[5] BEng Student, Mechanical and Aerospace Engineering, Carleton University, Ottawa, ON, Canada
[6] BEng Student, Mechanical and Aerospace Engineering, Carleton University, Ottawa, ON, Canada
[7] Professor of Aerospace Engineering, Mechanical and Aerospace Engineering, Carleton University, AIAA Member, Ottawa, ON, Canada.
[8] Professor of Aerospace Engineering, Mechanical and Aerospace Engineering, Carleton University, AIAA Member, Ottawa, ON, Canada.
[9] Professor of Aerospace Engineering, Mechanical and Aerospace Engineering, Carleton University, AIAA Member, Ottawa, ON, Canada.

1. Introduction

Over the past few decades, aircraft fuel efficiency was mainly improved by applications of refined aerodynamics, composite materials, structural optimization and enhanced engine performance. Yet, a step change towards that goal may be realized through designing novel aircraft configurations and considering new, additively manufactured, multifunctional materials and structural systems for significantly reducing green aircraft weight. Aircraft with BWB configuration are proposed for next generation of airliners, primarily due to their increased fuel efficiency and reduced acoustic footprint. BWB configuration blends the wings and fuselage into a single lifting surface which brings about several benefits including increased lift to drag ratio, decreased acoustic and environmental footprints [1,2, 4, 5] and increased fuel economy and payload. BWB configurations have been adopted in several civil, military, and academic applications. Examples include the research conducted by NASA and Boeing on the X-48 [6] and the Hyperion, a BWB UAV developed by a research team in Indiana [7, 8].

Carleton University BWB-UAV Capstone Project is concerned with the development of a functional BWB UAV to demonstrate the advantages of the BWB configuration versus fixed wing aircraft for the same payload. In this project, multiscale design optimization (MSDO) [8], an extension of topology optimization, is used to minimize the weight and increase the structural efficiency of the UAV. Using a detailed finite element model (DFEM), the geometry and structural components of the UAV are captured for the optimization process.

Using the Craig Bampton (CB) model order reduction method [14], the DFEM is reduced to a series of mass, stiffness, and damping matrices which are coupled to a doublet lattice aerodynamic model to generate the aeroelastic model required for the critical loads calculation. For each iteration of the MSDO, the matrices which define the mechanical response of the aeroelastic model are updated allowing for a computationally efficient method to integrate the dynamic aeroelastic response analysis into the MSDO algorithm.

Shape optimization [18] was also used to increase the structural efficiency of several interface mounts in the UAV including the motor mount without increasing the weight.

This paper presents a single design loop of the optimization process. First, an overview of the design is provided as a point of reference. The following sections define the initial detailed finite element model, the Craig-Bampton model order reduction, and the MSDO algorithm integrated with the aeroelastic response. To demonstrate the extent to which MSDO can reduce the weight of the UAV, preliminary MSDO results are presented. Lastly, shape optimization results are discussed and demonstrated.

2. Design Overview

The outer mold line (OML) of the BWB-UAV was defined using a NACA 4412 airfoil [9] which was modified to include a reflex in its camber required to increase the stability of the UAV and maximize its lift to drag ratio. As shown in Figure 1, the airframe of the UAV is divided into three components, namely, the wings, winglets, and fuselage. The wings are constructed using a multi-spar configuration. The cross sections of the spars are I-beams which are tapered along the span of the wings. The wings are connected to the fuselage and winglets using threaded fasteners and threaded inserts which are pressed into their respective mating components. Similarly, the skin is attached to the airframe using threaded inserts and fasteners which fasten flush to the outer surface of the skin, reducing the likelihood that the aerodynamic performance be impacted. Lastly, elevons are attached to the airframe and controlled through a universal ball joint.

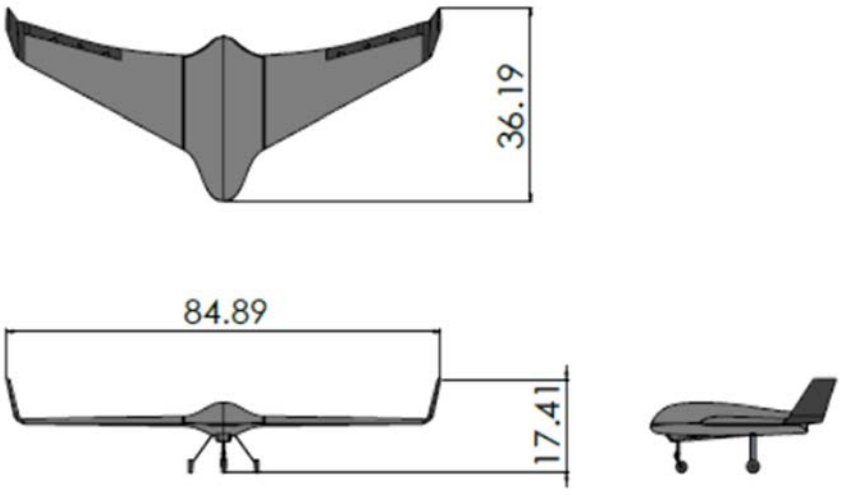

(a)

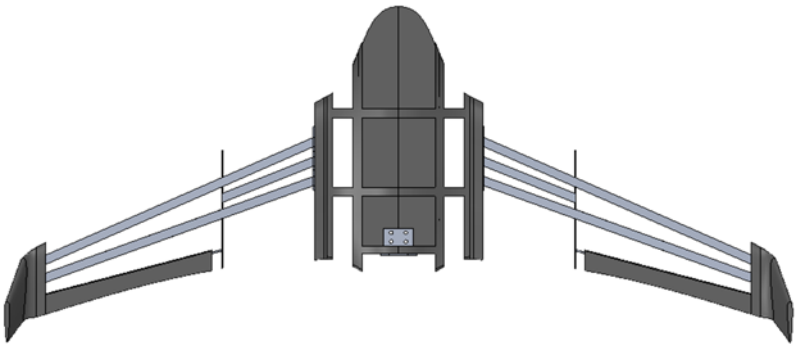

(b)

Figure 1: (a) Design envelope of the BWB-UAV OML and (b) airframe components (dimensions are in inches).

2.1 Material Properties

Four materials are used in the UAV [9]. The airframe is manufactured from Stratasys ABS M30 [19]. Aluminum 6061-T6 [11] is used to machine the landing gear and polylactic acid (PLA) [20] is used to manufacture the motor mount. The skin is manufactured from a carbon fiber composite. Specifically, a one-layer (0° angle orientation) composite reinforced with twill weave fibers [10]. Fused deposition modeling is used to build the airframe and motor mount, the landing gear are manufactured using CNC machining, and the skin is manufactured using vacuum assisted resin transfer molding [21].

The material properties defined in Table 1are used to characterize the mechanical response of the UAV in the DFEM. 3D printed materials have anisotropic properties where material mechanical properties are dependent on the print orientation [9]. To be conservative, the material properties of the print orientation which yielded the minimum strength are listed for ABS M30. However, because of the significant difference between the PLA material properties for the different print orientations, the properties of the maximum strength were selected. Lastly, the material properties provided by the supplier [10] were used to model the carbon fiber epoxy composite and A-basis material properties from [11] were used to model Al 6061-T6. Because the skin is manufactured using a twill weave fiber, the in-plane material properties are isotropic. Hence, only one property is listed in Table 1.

Table 1: UAV material properties.

Material Property	**ABS M30**	**PLA**	**Al 6061-T6** [11]	**Carbon Fiber (Twill) Epoxy Composite** [10]
Elastic Modulus [ksi]	290	500	9,901	2,466
Poisson's Ratio	0.35	0.35	0.33	0.77
Density [slug/in^3]	0.0012	0.0013	0.00303	0.0018
Yield Strength [ksi]	N/A	4.3	35.0	N/A
Tensile Strength [ksi]	3.0	7.5	42.0	15.9

Furthermore, a structural damping ratio of 3.0% was assumed for all materials.

2.1.1 Thermal stability ABS M30 and PLA

While ABS M30 is a cost-effective material, a more widely available and less expensive alternative is PLA. Both materials are equally good options to manufacture the airframe of the UAV. Our experimental investigation showed that the strength properties of PLA even surpass those of ABS M30 at room temperature, see Figure 2. However, the thermal stability of the two materials varies quite significantly.

A series of tensile specimen were tested in accordance with ASTM D368 [22] at 68°F (room temperature), 107°F, and 140°F. The results indicated that ABS M30 is significantly more stable than PLA (see Figures 2 through 4). At room temperature, PLA was able to sustain a larger tensile load then ABS M30; however, as the temperature increased, the PLA tensile response continuously decreased while the tensile response of ABS M30 remained relatively constant. In the selected temperature range, the strength of the PLA decreased by approximately 77%. Based on the thermal stability of PLA and ABS M30, ABS M30 was selected as the material to manufacture the airframe.

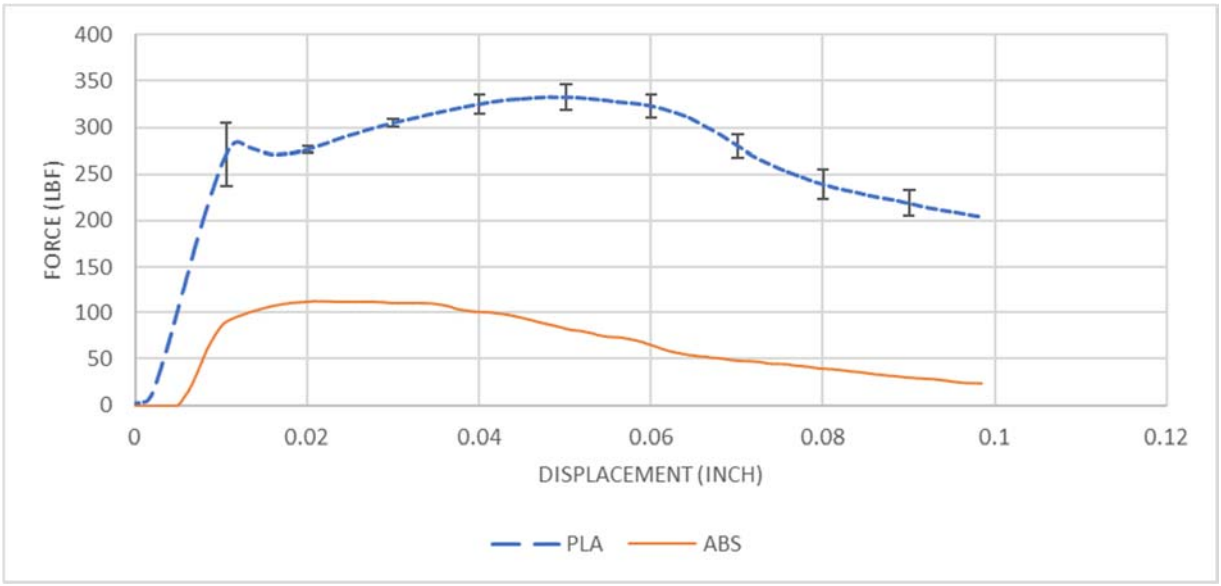

Figure 2: ABS M30 / PLA thermal stability test (68°F)

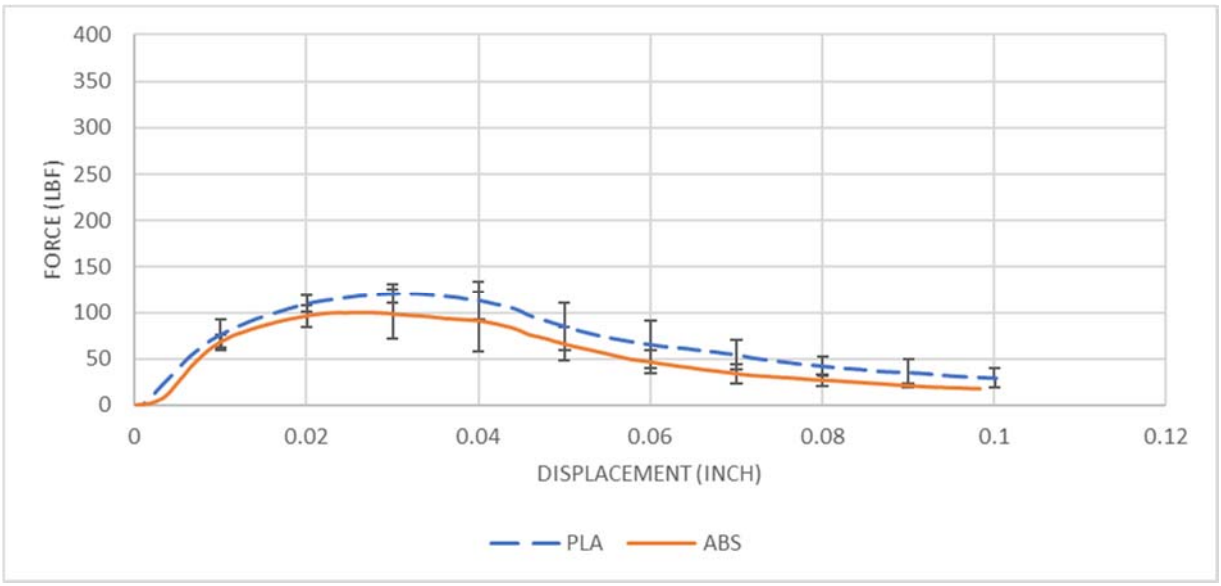

Figure 3: ABS M30 / PLA thermal stability test (107°F)

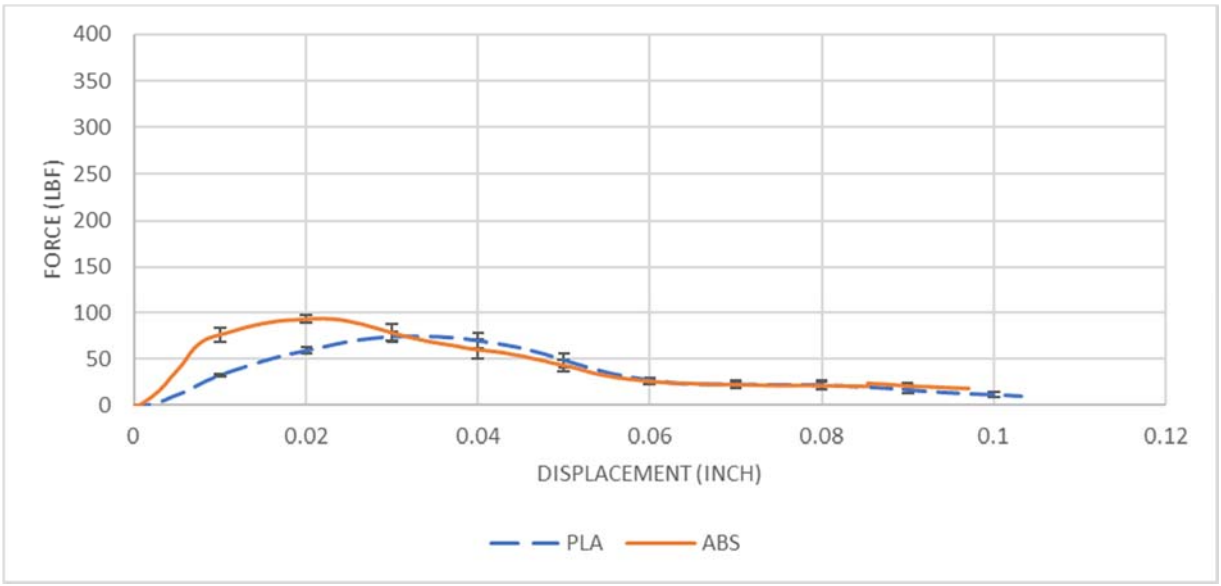

Figure 4: ABS M30 / PLA thermal stability test (140°F)

Because the UAV is still in development, the payload is currently limited to the motor, battery, and the avionics. However, the battery and motor are the primary sources of weight. As a result, the analysis described in this paper will only consider the effects of the battery and motor as concentrated masses as well as the airframe distributed weight represented by material density distribution.

3. BWB-UAV Finite Element Model Development for MSDO

The DFEM (see Figure 5) is used to analyse the stresses induced in the BWB-UAV and verify the sizing of the components and conduct the MSDO. While the DFEM does not require specific inputs to serve as a stress model, the MSDO does require specific parameters be built into the FEM. The finite element parameters which pertain to MSDO include the designation of design and non-design spaces and the element sizing parameters.

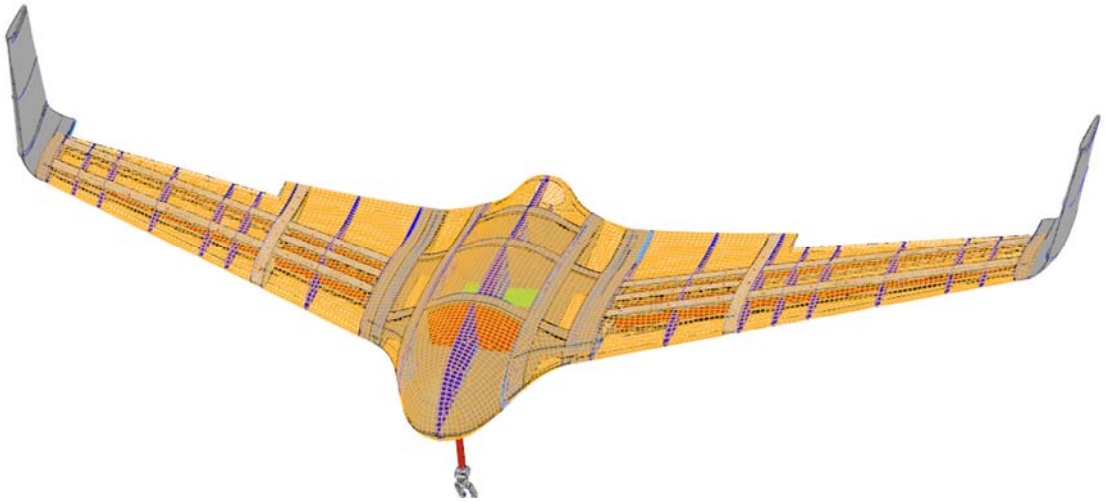

Figure 5: The BWB-UAV DFEM

In the ABS airframe, three sets of design spaces were defined. The vertical webs of the spars, the walls of the fuselage, and the inside of the winglets were sectioned from the model and defined as design spaces (see Figure 6).

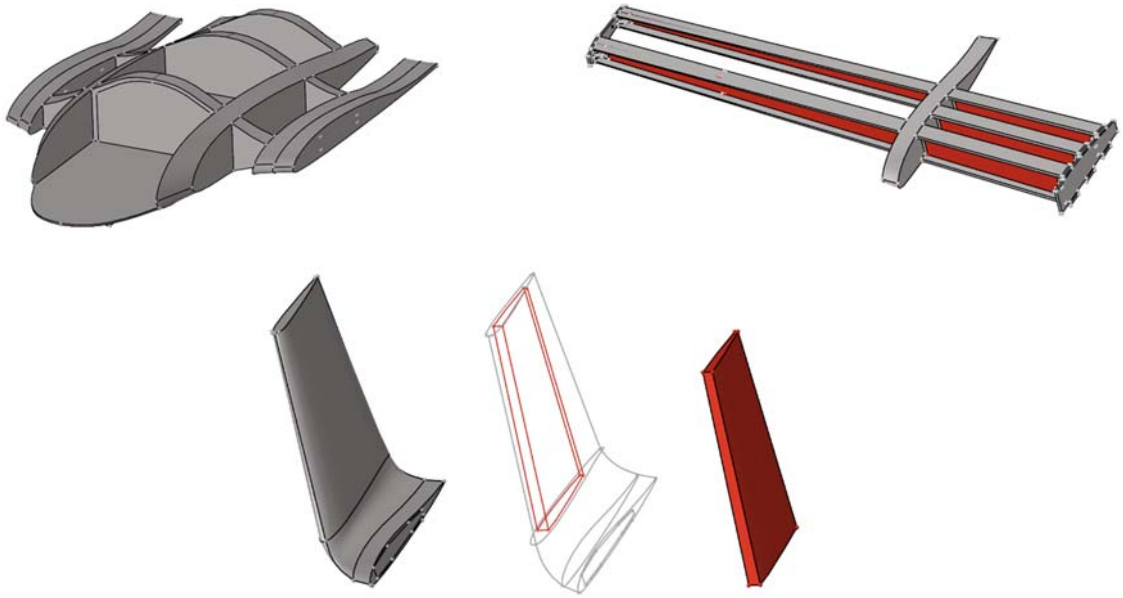

Figure 6: The BWB-UAV ABS airframe design spaces

Based on the element type specified in the DFEM design spaces, the lattice topology implemented in the design spaces shown in Figure 6 can be controlled. Two common unit cells are shown in Figure 7, namely the Kelvin and Octet cells [12]. The Kelvin cell is a bending-dominated unit cell which converts macroscopic loads into bending loads in its microscopic members. The bending deformation allows for the significant increase of the energy absorption characteristics of materials microscopically architectured with Kelvin cell [12]. On the other hand, the octet unit cell is a stretch-dominated unit cell which induces tensile/compressive loads in its members. The unique property of the octet cell is that it yields a high specific stiffness [12]. Hence, the octet unit cell can be used to minimize the mass of the airframe while minimizing the impact on the airframe's stiffness and, therefore, its aerodynamic efficiency. The octet cell can be introduced in the airframe using second order tetrahedral elements.

(a) (b)

Figure 7: MSDO lattice structure unit cell structure of the (a) Kelvin cell and (b) octet truss [13].

3.1 Lattice Tensile Tests

Because the octet cell is able to maintain and even increase the specific stiffness of the structure, the octet cell was used in the airframe optimization described in section 4. Using the octet cell to optimize the airframe will reduce the aeroelastic implications of the optimization process. A series of tensile tests were conducted using ASTM D638 [17] Type III specimen to verify the mechanical properties of the octet truss relative to an un-optimized tensile specimen made of solid material (see Figure 8).

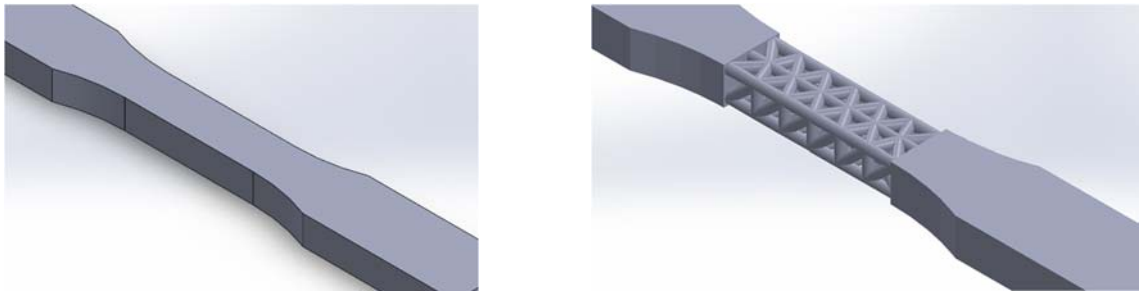

(a) (b)

Figure 8: (a) Unoptimized/Solid and (b) optimized/lattice tensile specimen.

Using a strain rate of 5 mm/min and Material Testing System (MTS) machine, the tensile response of the unoptimized and optimized specimen are shown in Figure 9. The results of the tensile tests confirm that the mechanical response of ABS M30 is maintained in the optimized specimen. The maximum tensile strength and elastic modulus of the unoptimized tensile specimen were approximately 4.6 ksi and 290 ksi, respectively. The maximum tensile stress and elastic modulus of the optimized specimen were 4.7 ksi and 667.1 ksi.

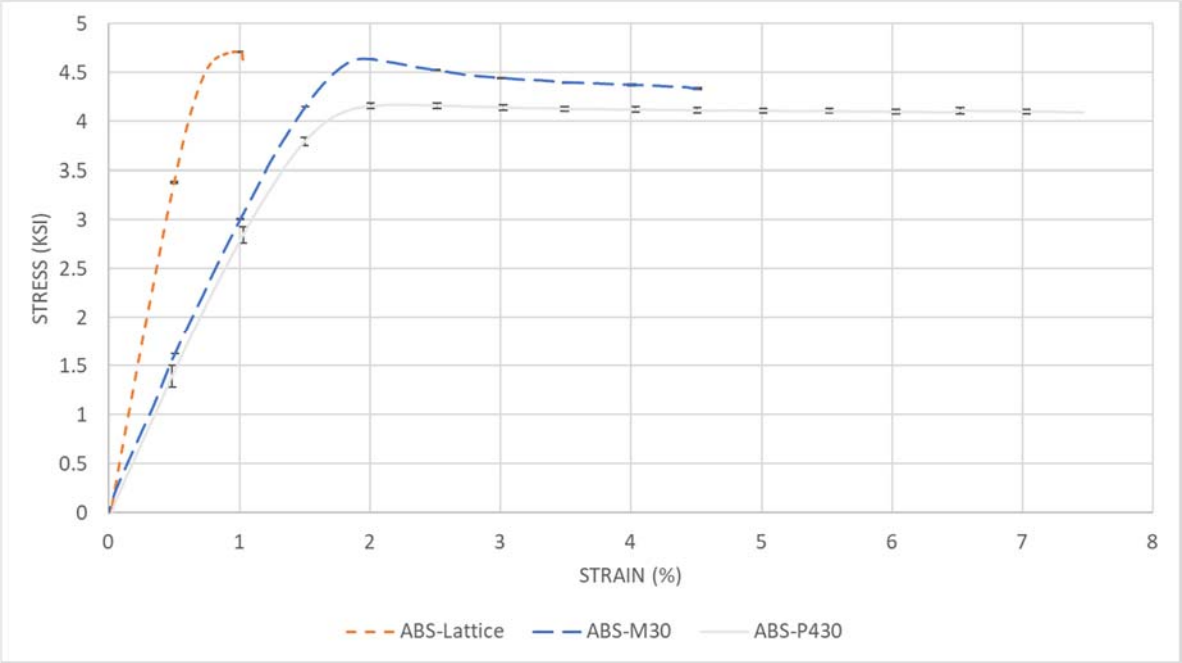

Figure 9: Tensile stress-strain comparison of solid ABS M30 and ABS M30 optimized using the octet cell.

Because the octet cell is a stretch-dominated lattice structure, the elastic modulus of the parent material increased when the un-optimized tensile specimen was replaced with an array of octet cells. In this case, the stiffness increased by 56%. The increase in stiffness is also evident in the plastic response of the material. When the tensile load exceeded the ultimate strength of the solid specimen, the plastic response of ABS M30 was approximately 50% of the total response (i.e. the sum of the elastic and plastic portions). The optimized specimen, because of its increased stiffness, essentially fractured at its ultimate strength. Another factor which contributed to the limited plasticity in the optimized specimen are the stress concentrations created by joining lattice members.

3.2 Craig-Bampton Model Order Reduction

While the optimization process varies the mass and stiffness properties of the UAV which changes the dynamic response of the UAV; therefore, the aeroelastic response of the UAV must be reanalyzed to determine if critical aeroelastic loads change significantly. If the aeroelastic loads increase, the amount of material removed from the airframe may have to decrease to support the revised loads. If the opposite occurs and the aeroelastic loads decrease, this signifies that additional material may be removed from the airframe. Although the DFEM will continuously capture the changing mass and stiffness distribution of the UAV, using a DFEM to determine the aeroelastic response of the UAV is computationally expensive.

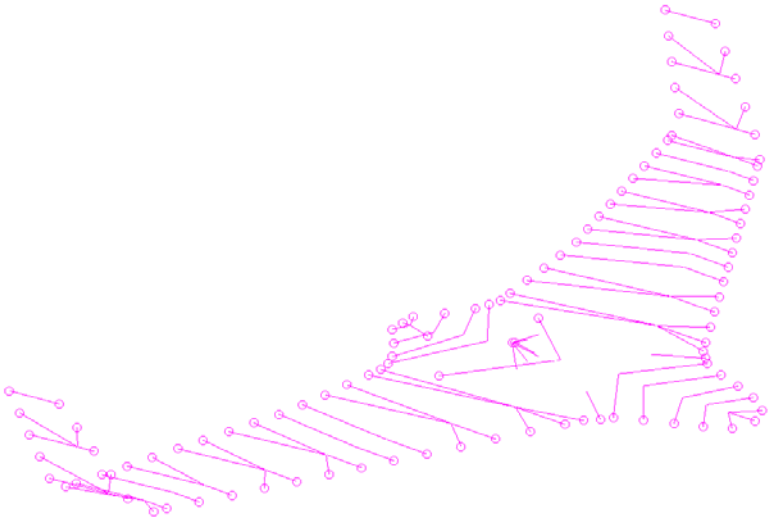

Figure 10: The BWB-UAV aeroelastic FE model.

The Craig-Bampton (CB) model order reduction is used to condense the FEM of the UAV to a series of mass, stiffness, and damping matrices with smaller retained set of degrees of freedom. In addition to eliminating the need to include the geometric and material properties in the aeroelastic model, the CB model reduction also reduces the degrees of freedom required which must be resolved to compute the response of a structure to an external input [14]. The CB model reduction increases the computational efficiency of the aeroelastic model by limiting the model reduction to the natural frequencies / mode shapes below 100 Hz. The modes above 100 Hz can be truncated because they typically contain too little energy to induce any significant deformation in the airframe [15] and will, therefore, induce a negligible aeroelastic response. Using the CB model reduction, the unoptimized DFEM was reduced from 4,885,134 degrees of freedom to 216 degrees of freedom.

To verify the fidelity of the CB reduced order model, its natural frequencies and mode shapes were compared to those of the DFEM. The acceptance criterion was defined as a maximum percent difference of 5% in natural frequencies. Except for the rigid body modes of the two models, the percent difference between the natural frequencies of the elastic modes was well below 5.0% (see table 2). The elastic mode shapes of the two models were also compared. For reference, mode 8 of the DFEM and aeroelastic model are shown in Figure 11.

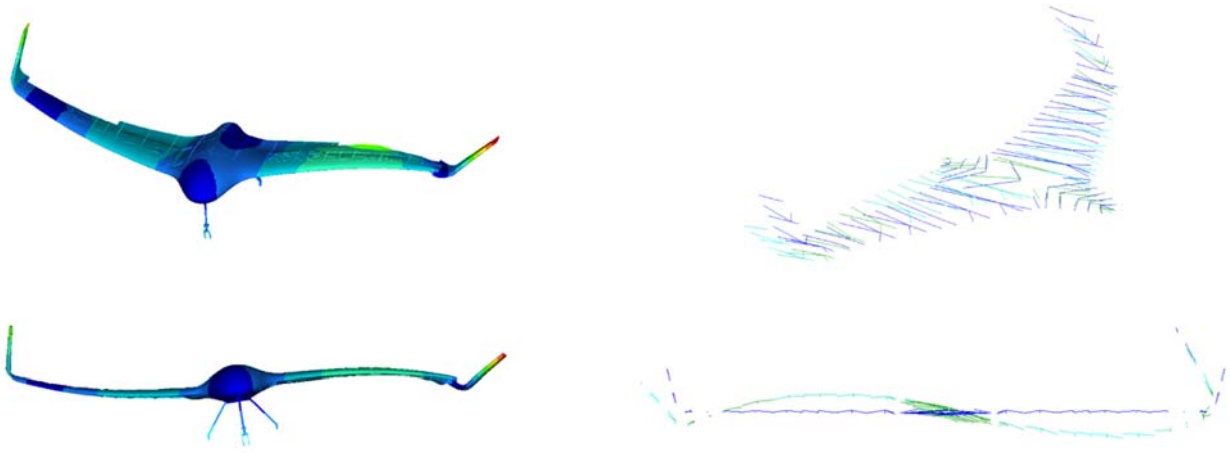

(a) (b)

Figure 11: Mode 8 (7.2 Hz) deflection comparison between (a) the DFEM and (b) the aeroelastic model.

Table 2: Natural frequency comparison of the DFEM and aeroelastic models

Mode No.	Natural Frequencies [Hz]		Percent Difference (DFEM-DMIG)
	CB Model (DMIG)	DFEM	
1	3.94	3.94	0.0%
2	7.28	7.28	0.0%
3	9.01	9.01	0.0%
4	11.71	11.70	0.0%
5	15.34	15.33	0.0%
6	18.18	18.18	0.0%
7	18.89	18.89	0.0%
8	19.28	19.28	0.0%
9	24.61	24.59	0.1%
10	26.94	26.94	0.0%
11	27.94	27.94	0.0%
12	28.85	28.80	0.1%
13	31.64	31.61	0.1%
14	32.05	32.04	0.0%
15	34.73	34.73	0.0%
16	36.64	36.64	0.0%
17	36.71	36.71	0.0%
18	37.33	37.33	0.0%
19	38.24	38.23	0.0%
20	38.35	38.35	0.0%
21	38.91	38.91	0.0%
22	39.31	39.31	0.0%
23	41.91	41.91	0.0%
24	43.09	43.08	0.0%

3.3 Aeroelastic Model

Because the mechanical response of the aeroelastic model is derived from the DFEM using the CB model reduction, the aeroelastic model (see Figure 10) was developed using a series of nodes along the elastic axis of the wings of the UAV and along the axis of symmetry of the fuselage. The nodes are used to couple the mass, stiffness, and damping matrices from the CB model reduction to structural mesh of the aeroelastic model. The structural mesh of the aeroelastic model is then superimposed with an aero-panel mesh (see Figure 11) to create a FE model which couples the aerodynamics and mechanical responses of the UAV.

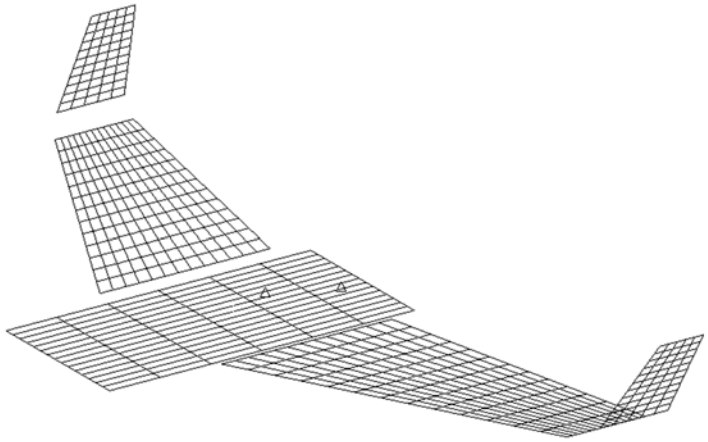

Figure 11: The BWB-UAV aero-panel mesh

The aero-panel mesh employs 2D potential theory and the Doublet Lattice Method (DLM) [23] to simulate the aerodynamics of the UAV.

3.3.1 Aeroelastic Response Analysis

To determine the critical loads of the UAV, the Federal Aviation Regulations certification (FAR-25) [16] are used. Various load cases are analysed based on the mission profile of the UAV, including its maneuver and center of gravity envelopes. The critical dynamic and static load cases were defined based on, respectively, 1g flight conditions and aerodynamic turbulence modeled using Power Spectral Density (PSD) and Tuned Discrete Gust (TDG) gust conditions [24]. MSC NASTRAN [25] is used for the gust analysis.

4. Aeroelastic-Optimization Design Loop

The aeroelastic response of the unoptimized configuration of the UAV was analyzed in depth. However, once optimized, the mass and stiffness parameters of the airframe of the UAV will change due to the apparent material properties of the graded lattice structure. Consequently, the aeroelastic analysis must be updated after the UAV has been optimized to determine if the loads have increased or decreased as a result of the change in the structural characteristics and thus its response. The interaction between the MSDO and aeroelastic analysis defines a design loop which must be conducted to produce a fully optimized design.

Figure 13 shows the design optimization loop considered. Using the unoptimized configuration of the UAV, the DFEM is used to generate the unoptimized mass, stiffness, and damping matrices. The CB matrices are passed to the aeroelastic model and the PSD and TDG loads analyses are conducted. Using the initial set of aeroelastic loads superimposed with the 1g flight loads, the MSDO is conducted on the DFEM. The optimized structure is then used to update the CB reduction matrices and the aeroelastic response of the UAV is reevaluated. The optimization and aeroelastic analyses are repeated until the convergence criteria is met. Convergence was defined as the point at which the magnitudes of the loads calculated from the aeroelastic analysis varies by less than 2% of the initial loads.

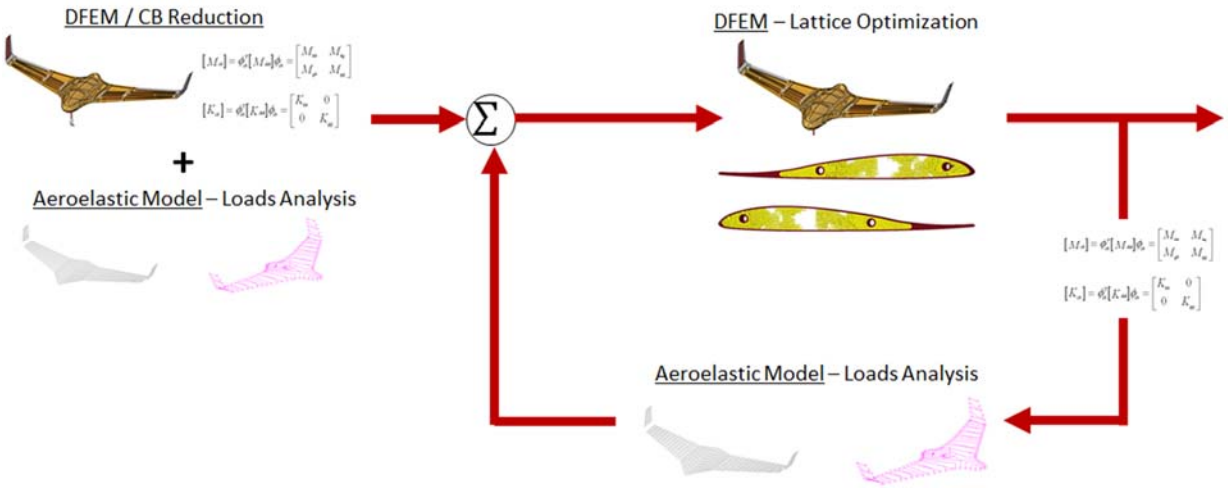

Figure 12: MSDO-Aeroelastic CB model reduction design loop.

4.1. Multiscale Design Optimization

MSDO is a two-stage optimization process which combines topology optimization [26] (i.e. a macroscale optimization) with lattice optimization [27] which occurs at the microscale. While macroscale optimization is used to remove material from the airframe outside of the critical load paths, the microscale optimization is used to increase the structural efficiency by replacing the material along the critical load paths with a functionally graded lattice structure. The lattice structure is composed of a series of repeating unit cells. When implemented in place of the solid material, the members of the cells are placed in pure tension or compression. Therefore, the stress is maximized in the cross-sections of the materials, whereas the solid material from the topology optimization may be in bending. In bending, the maximum stress occurs solely along the surface.

4.2 Optimization constraints

The optimization statement used to optimize the airframe of the UAV is defined in equation (1). Mass minimization is the objective function and the relative densities of the finite elements serve as the design variables. The optimization constraints include two geometric and two structural constraints. The geometric constraints include a minimum volume fraction of 0.3 to increase the stability of the optimization algorithm and a manufacturing constraint (i.e. a minimum dimension of 1.5 mm). The manufacturing constraint ensures the lattice is manufacturable and the structural integrity of the lattice is uncompromised due to the dimensional stability of the manufacturing process. The structural constraints include a von Mises stress constraint and a safety factor of 1.5 was applied to the critical buckling loads to prevent any microscopic buckling in the lattice.

$$
\begin{aligned}
&min.\{ && m(x) && \textit{Airframe mass} \\
&s.t.\begin{cases} && 0.1 < \bar{\rho} < 0.8 && \textit{Elemental relative density} \\ && V > 0.3 && \textit{Design space volume fraction} \\ && r_{\,lattice} > 1.5\ mm && \textit{Lattice min. radius} \\ && p \approx 1.25 && \textit{Density penalization (i.e. porosity)} \\ && \sigma_{vM} < S_{allowable} && \textit{Max allowable stress} \\ && SF_{buckling} = 1.5 && \textit{Buckling safety factor} \end{cases}
\end{aligned}
\tag{1}
$$

The optimization constraints defined in equation (1) are purposely underdefined to maximize the output from the optimization. Although the lattice optimization poses some aeroelastic concerns (e.g. divergence and flutter), it is good practice not to over constrain the optimization [2]. Rather, the additional constraints used to control the aeroelastic response of the optimized UAV should be developed as the aeroelastic-optimization loop defined in section 4 progresses.

4.3 Boundary Conditions and Applied Loads

Although the UAV is unconstrainted in flight, in order to analyze the effect of the aeroelastic loads and optimize the airframe a constraint must be applied. The axels of the landing gear were used to constrain the DFEM. RBE2 elements [25] were used to create a single node about which the landing gear could be constrained in all degrees of freedom (see Figure 13). These constraints were selected because the primary focus of the analysis is to optimize the airframe of the UAV. Although the selected constraints induce unrealistic stresses in the landing gear, constraining the landing gear minimizes adding any excessive stiffness to the airframe.

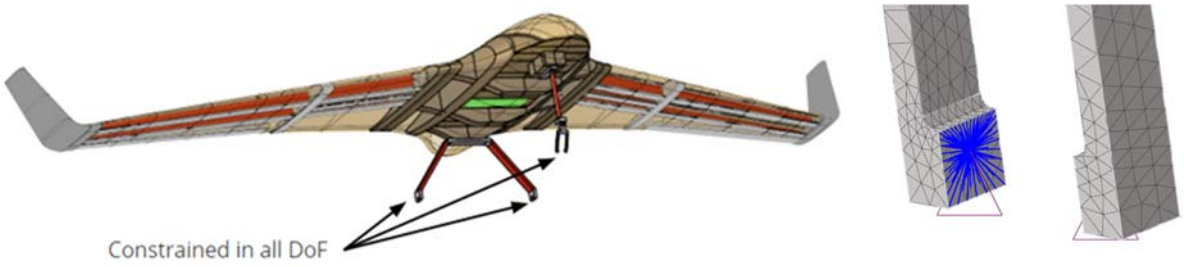

(a) (b)

Figure 13 : DFEM MSDO constraints (a) general view (b) example of the single point constraint applied to the RBE2 of the nose landing gear.

4.4 Preliminary MSDO Results

Using critical load case identified in section 3.3.1., the geometric constraints defined in section 4.1, and the optimization constraints defined in section 4.2, MSDO was conducted on the airframe of the UAV. The fuselage and the spars were the focus of the preliminary optimization. Using MSDO the weight of the spars and fuselage was reduced by 32% and 40%, respectively. The optimized spars are shown in Figure 14.

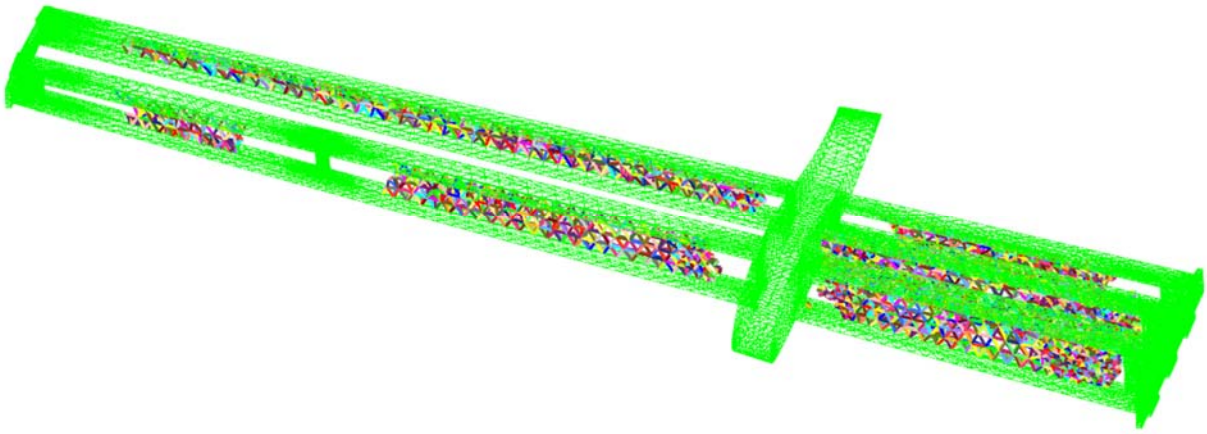

Figure 14: Preliminary results of the MSDO of the ABS Spars of the UAV

The unoptimized weight of the UAV is 23 lb_m. Based on the preliminary results, the optimized weight of the UAV is 18.3 lb_m. These results do not account for the aeroelastic loads the structure must be able to sustain. However, based on the trends observed in these analyses and the results from the previous MSDO of the multi-rib configuration of the UAV [1], it is projected that a weight reduction up to 43% of the unoptimized weight can be achieved.

5. Shape Optimization

As discussed in section 1. Shape optimization [18] was used to increase the structural efficiency of the motor mount. The motor mount essentially served as a standoff to offset the motor prop from the skin of the BWB-UAV. The initial design of the motor mount was a double flanged design connected using semi-circular legs (see Figure 15).

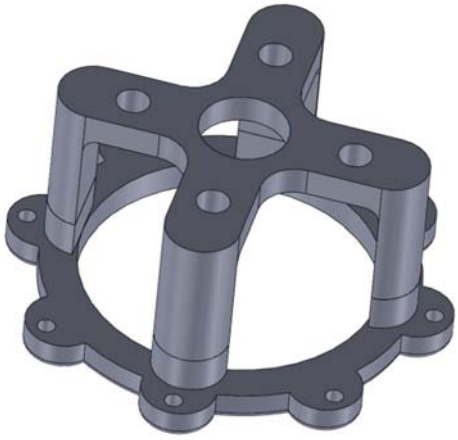

Figure 15: The UAV motor mount – semi-circular legs

The structural capacity of this design was verified by conducting compression tests and comparing the results to the expected thrust load of the motor. The expected thrust of the motor was 20.3 lb_f and the compression tests revealed that the motor mount could sustain an average load of 285 lb_f. Although the structural capacity of the motor mount exceeds the design requirements of the BWB-UAV, the test results indicated that the motor mount would fail through buckling. Buckling is an elastic failure mode, meaning that the plasticity of the material is not utilized. Hence, buckling is not a structurally efficient failure mode [18].

Using shape optimization and shape transformers [18], the geometric efficiency of the legs was increased in order to increase the structural efficiency. The geometric efficiency provides an indication of the likelihood that the geometric properties of a given cross-section will induce failure due buckling (a mode of failure which results from bending) or due to yielding. The geometric efficiency is defined as the ratio of the second moment of area of the cross-section normalized with respect to the second moment of area of a square which encapsulates the cross-section to the area of the cross-section normalized with respect to the area of the enclosing square [18] That is, as the bending stiffness of the cross section increases, the geometric efficiency increases, and the likelihood that the cross-section will fail due to buckling will decrease. Ideally, the optimization process would force the legs to yield and fail due to plastic rupture. A diamond cross-section was selected for the second iteration of the motor mount (see Figure 16).

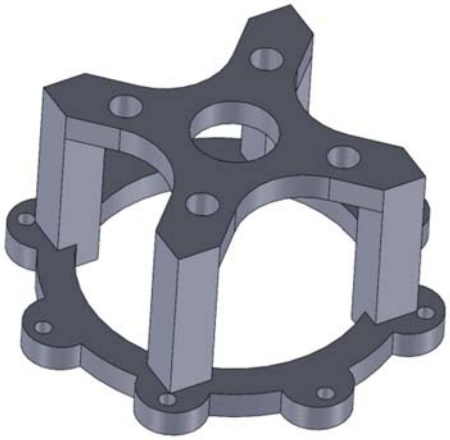

Figure 16: The UAV motor mount – diamond cross-section

The cross-sectional area of the legs was maintained constant from the original design to avoid increasing the mass of the motor mount. The geometric properties of the two cross-sections are summarized in Table 3. The geometric

efficiency of the diamond cross-section is significantly higher than that of the semi-circle and, therefore, indicates that the square cross-section is more likely to fail due to plasticity, rather than buckling.

Table 3: Motor mount shape optimization parameters.

Cross-sectional Geometry	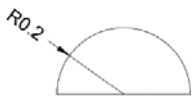	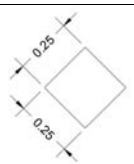
Cross-Sectional Area (mm^2)	0.061	0.061
Second Moment of Area (mm^4)	1.65×10^{-4}	3.07×10^{-4}
Normalized Second Moment of Area (ψ_I)	0.08	0.25
Normal Cross-Sectional Area (ψ_A)	0.69	0.50
Geometric Efficiency ($\lambda = \frac{\psi_I}{\psi_A}$)	0.12	0.50

To verify that the change in cross-section would increase the efficiency of the motor mount, the revised design also underwent compression testing. Comparing the results of the nominal and optimized configurations of the motor mount (see Figure 17), it is evident that the change in cross section increased the structural capacity of the motor mount by a factor of 5.4. Previously, the maximum sustainable load was 285 lb_f. The revised design can sustain a compressive load of 1562 lb_f. Figure 17 proves that the failure mode of the motor mount has also changed. The force required to deform the motor mount decreases after yielding; in contrast, the response of the unoptimized motor mount plateaus before failure, a characteristic of elastic buckling.

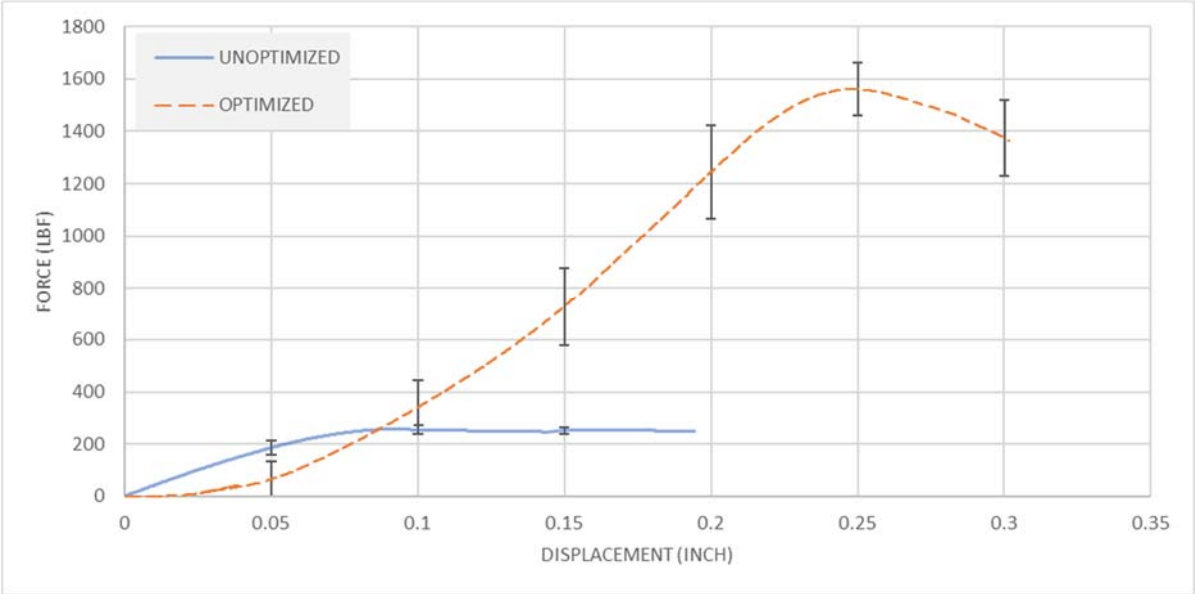

Figure 17: Motor mount compression test – shape optimization results

Based on the results of this analysis, the shape optimization was successful in yielding a more efficient design. Although the failure load of the optimized motor mount is significantly higher than the design load, modifying the design to reduce the weight of the motor mount will yield diminishing returns. Furthermore, the mass of the motor mount (i.e. 0.027 lb_m) is insignificant relative to the other structural components of the BWB-UAV.

6. Conclusion

The work presented in this paper demonstrates the feasibility of integrating the aeroelastic response analysis into the MSDO algorithm. Using the CB model order reduction, the DFEM of the BWB-UAV was reduced and coupled to a doublet lattice aerodynamic model of the UAV to generate a computationally efficient aeroelasticity module. Using this process, a critical load case was analyzed and demonstrated that a 43% weight reduction in the airframe can be achieved using MSDO.

The aeroelastic-optimization algorithm presented in this paper will be completed to convergence to maximize the optimization in the following years. Once complete, the airframe of the BWB-UAV will be 3D printed, assembled, and flown to gauge its performance.

Acknowledgments

Special thanks to Bombardier Aerospace, Carleton University Engineering Student Equipment Fund (CUSEF), Agile Manufacturing and the rest of the BWB UAV project team who provided aid, tools, materials, guidance, and mentorship.

References

[1] R. Liebeck, M. Page and B. Rawdon, "Blended-wing-body subsonic commercial transport," 1998.

[2] Z. Lyu and J. R. Martins, "Aerodynamic Design Optimization Studies of a Blended-Wing-Body Aircraft," *Journal of Aircraft,* vol. 51, no. 5, pp. 1604-1617, 2014.

[3] R. Liebeck, "Design of the Blended Wing Body Subsonic Transport," *Journal of Aircraft,* vol. 41, no. 1, pp. 10-25, 2004.

[4] S. Siouris and N. Qin, "Study of the effects of wing sweep on the aerodynamic performance of a blended wing body aircraft," *Proceedings of the Institution of Mechanical Engineers Part G, Journal of Aerospace Engineering,* vol. 221, pp. 47-55, 2007.

[5] F. Wang, Artist, *The comparison of aerodynamic and stability characteristics between conventional and blended wing body aircraft.* [Art]. Cranfield University, MSc thesis, January 2012.

[6] Nasa.gov, "NASA - The X-48B Blended Wing Body," 2018. [Online]. Available: https://www.n asa.gov/topics/aeronautics/features/bwb_main.html. [Accessed 18 February 2018].

[7] J. Koster, A. Velazco, C. Munz, E. Kraemer, K. Wang and D. Verstraete, "Hyperion UAV: An International Collaboration," *50th AIAA Aerospace Sciences Meeting including the New Horizons Forum and Aerospace Exposition,* 2012.

[8] J. Koster, "The Hyperion 2.1 Green Aircraft Project," in *51st AIAA Aerospace Sciences Meeting including the New Horizons Forum and Aerospace Exposition*, Dallas, 2013.

[9] "M. Dinovitzer, C. Miller, A. Hacker, G. Wong, Z. Annen, P. Rajakareyar, J. Mulvihill, and M.S.A. ElSayed. "Structural Development and Multiscale Design Optimization of Additively Manufactured UAV with Blended Wing Body Configuration Employing Lattice Materials", AIAA Scitech 2019 Forum, AIAA SciTech Forum, (AIAA 2019-2048)

[10] Performance Composites, "Mechanical Properties of Carbon Fibre Composite Materials, Fibre / Epoxy resin (120°C Cure)," Performance Composites, [Online]. Available: http://www.performancecomposites.com/carbonfibre/mechanicalproperties_2.asp?fbclid=IwAR1iRUL8RrZI0tWmDlUKpHg5BeioRdZVdBaKbfw8qslqeKHfKqw0Rfgs5l0. [Accessed 21 January 2019].

[11] Battelle Memorial Institute, Metallic Materials Properties Development and Standardization (MMPDS), Washington: Federal Aviation Administration, 2016.

[12] P. Chopra, "Effective Mechanical Properties of Lattice Materials," University of British Columbia, Vancouver, 2011.

[13] X. Zheng, "Ultralight, ultrastiff mechanical metamaterials," *Science (New York, N.Y.),* vol. 344, pp. 1373-1377, 2014

[14] Siemens, Superelement User's Guide, TAUCS, 2014.

[15] T. J. Young, "Primer on the Craig-Bampton Method - An introduction to boundary node functions, base shake analyses, load transformation matrices, modal synthesis and much more," 2000.

[16] "Electronic Code of Federal Regulations," 27 March 2018. [Online]. Available: https://www.ecfr.gov/cgi-bin/textidx?node=14:1.0.1.3.11. [Accessed 15 March 2018].

[17] ASTM International, "ASTM D638-14, Standard Test Method for Tensile Properties of Plastics," 2014. [Online]. Available: www.astm.org.
[18] M.S.A. ElSayed, "Multiscale structural design of columns made of regular octet-truss lattice material," International Journal of Solids and Structures, vol. 47, no. 14-15, pp. 1764-1774, 2010.
[19] Croccolo, Dario, Massimiliano De Agostinis, and Giorgio Olmi. "Experimental characterization and analytical modelling of the mechanical behaviour of fused deposition processed parts made of ABS-M30." Computational Materials Science 79 (2013): 506-518.
[20] Drumright, Ray E., Patrick R. Gruber, and David E. Henton. "Polylactic acid technology." Advanced materials 12.23 (2000): 1841-1846.
[21] Sadeghian, Ramin, et al. "Manufacturing carbon nanofibers toughened polyester/glass fiber composites using vacuum assisted resin transfer molding for enhancing the mode-I delamination resistance." Composites Part A: applied science and manufacturing 37.10 (2006): 1787-1795.
[22] ASTM D368: Standard Test Method for Tensile Properties of Plastics.
[23] Albano, Edward, and William P. Rodden. "A doublet-lattice method for calculating lift distributions on oscillating surfaces in subsonic flows." AIAA journal 7.2 (1969): 279-285.
[24] Hoblit, Frederic M. Gust loads on aircraft: concepts and applications. American Institute of Aeronautics and Astronautics, 1988.
[25] McCormick, Caleb W. "The NASTRAN User's Manual (Level 15)." (1972).
[26] Bendsøe, Martin P. Topology optimization. Springer US, 2009.
[27] M.S.A. Elsayed. Multiscale mechanics and structural design of periodic cellular materials. Diss. McGill University Library, 2010.